

High-resolution water-saturation prediction using geostatistical inversion and neural network methods

Islam A. Mohamed¹, Mahmoud Hemdan¹, Ahmed Hosny¹, and Mohamed Rashidy¹

Abstract

One of the main challenges that we face is the accurate prediction of pore-fluid properties with the highest possible resolution. The seismic resolution is the most limiting factor, especially in our case, in which the main reservoirs are deepwater turbidite channels and their thin beds typically fall below the seismic tuning thickness. Therefore, we designed a new workflow that combines the geostatistical inversion and the neural network analysis with the aim of predicting a 3D high-resolution water saturation (sampled every 1 ms), overcoming the limitation of seismic detectability and providing better reservoir characterization. The power of the geostatistical inversion is that it provides multiple model realizations, and each realization honors the well data (statistical information and logs) and the seismic data. These realizations are more reliable and high-resolution versions of the elastic parameters. On the other hand, the main advantage of the neural network is that it establishes a stable nonlinear link between the input seismic and inversion results and the target water saturation. The available data set for this study includes three angle stacks and seven wells from Scarab field, offshore Nile Delta. The resulted high-resolution saturation volume was tested using blind-well analysis and revisit post the drilling of a new well later on. It gave spectacular results in both cases. The normalized correlations between the predicted saturation volume and the real saturation logs are 0.87 and 0.89, respectively. The results prove the validity of the workflow to accurately predict water saturation with a higher resolution than ever before.

Introduction

High-resolution reservoir characterization has always been a challenging task due to seismic resolution limitation. This challenge is particularly relevant when dealing with heterogeneous and complex deepwater turbidite reservoirs such as Scarab field, offshore Nile Delta. The Scarab's gas-charged sandstones consist of a Pliocene deepwater turbidite system forming complicated reservoirs. These reservoirs are characterized by the great variability of the thickness and the quality of the sand. In addition, the thin-bed gas sands usually smaller than the seismic vertical resolution. Previously, we used to implement the deterministic prestack seismic inversion method for lithology and fluids description and probabilistic neural network (PNN) for porosity and water-saturation prediction. Mohamed et al. (2014, 2017) present examples of the prediction of elastic properties and water saturation using prestack inversion and PNN. Notwithstanding, the deterministic inversion method provides a single nonunique solution. Moreover, it is restricted to the seismic data frequency band limits. Consequently, the accuracy of the reservoir static model is not optimum, and the calculated gas initially in place is

not consistent with the production data. Therefore, we needed to design a new workflow to overcome these limitations. The proposed workflow includes stochastic inversion and neural network methods. The stochastic approach proved its validity and accuracy through numerous published case studies (Moyen and Doyen, 2009; Araman et al., 2011; Samantaray et al., 2014; Pereira et al., 2017) as well as the neural network methods (Hampson et al., 2001; Herrera et al., 2006; Dumitrescu and Lines, 2009; Mohamed et al., 2014, 2017).

First, the stochastic inversion approach addresses the nonuniqueness and seismic resolution problems by generating variogram models (vertical and horizontal) from the high-frequency well-log data and combines it with the band-limited seismic data. Accordingly, it generates high-frequency realizations for each of the elastic properties. Then, it ranks the stochastic realizations, assesses the uncertainty, and generates facies probability distributions (Bellatreche et al., 2017). Subsequently, the output elastic volumes and gas-sand probability are used to train neural networks to provide a high-resolution water-saturation volume.

¹RASHPETCO, Cairo, Egypt. E-mail: islam.ali@rashpetco.com; mahmoud.hemdan@rashpetco.com; ahmed.hosny@rashpetco.com; mohamed.mahmoud@rashpetco.com.

Manuscript received by the Editor 25 August 2018; revised manuscript received 13 December 2018; published ahead of production 22 January 2019; published online 18 March 2019. This paper appears in *Interpretation*, Vol. 7, No. 2 (May 2019); p. T455–T465, 13 FIGS., 1 TABLE.

<http://dx.doi.org/10.1190/INT-2018-0153.1>. © 2019 Society of Exploration Geophysicists and American Association of Petroleum Geologists. All rights reserved.

The main advantage of this workflow is to predict the high-resolution reservoir property without boosting noise. The proposed workflow, however, is not straightforward, and the accuracy of the estimates depends on several factors, such as the quality of data (including seismic and well-log data), processes and conditioning applied to these data, and inversion and neural-network parameters. The most limiting factors are the large memory requirements, and therefore the long running time for the geostatistical inversion, and also the need of multiple wells (not less than three wells) for the training of the neural network. We have managed to overcome the memory requirements and the running time problems by constraining the area of interest and running the process overnight. However, this workflow still needs at least three wells to be applied successfully.

The same data set that used previously by Mohamed et al. (2014, 2015) were used in this study because we are going to compare the elastic properties and water saturation obtained from the geostatistical inversion with that obtained from the deterministic inversion previously. The data set includes a seismic prestack time migration survey acquired over the West Delta Deep Marine (WDDM) in 2006, near (0° – 15°), mid (15° – 30°), and far (30° – 45°) partial angle stacks, and also a root-mean-square (rms) stacking velocity volume. The available seismic data cover approximately 200 km^2 . It has a re-

cording length of 1500 ms (two-way time) and a sampling interval of 4 ms. The survey's inline spacing is 9.37 m, whereas the crossline spacing is 12.5 m. The frequency content at the reservoir level is 5–60 Hz with a central frequency of 30 Hz. Two interpreted horizons were used to constrain the inversion results, representing the top and base of the channel 1 reservoir. Four of the development wells — Scarab Da, Db, Dd, and De — in addition to the exploration wells — Scarab 1 and 2 — are going to be used in the study. The last well, Scarab Dc, has been used as a quality control well and is used neither in the inversion nor in the neural network analysis. All wells are vertical and have a full suite of wireline logs.

Geologic setting

Currently, the offshore Nile Delta is considered one of the major gas provinces in the world. In 2010, the United States Geological Survey made an estimation for the Nile Delta Basin province. Kirschbaum et al. (2010) state that “a mean of 1.8 billion barrels of recoverable oil, 223 trillion cubic feet (TCF) of recoverable gas, and six billion barrels of natural gas liquids” would exist. In summer 2015, the Italian oil company (ENI) made the giant “Zohr” discovery. The Zohr-1 discovery well found a total of 654 m of continuous vertical biogenic gas column in a shallow-water carbonate facies that is aged Miocene and Lower Cretaceous. The subsequent appraisal wells confirmed the initial volumes in place estimated at 30 TCF (Cozzi et al., 2018). Hence, this discovery along with other recent discoveries proofs the remaining hydrocarbon potentiality of the offshore Nile Delta Basin.

Apart from the carbonate (Zohr) play, the primary target for hydrocarbon exploration and development is the deepwater channel systems. Those turbidite channel systems are mainly deposited in a slope to basin-floor setting, occupying the outer part of the Nile Delta Cone. The sediments of the Nile Delta Basin extended from late Paleogene to Pleistocene (Aal et al., 2001). The Pliocene-Pleistocene sequences represent a thick part of the sediments (exceed 3 km) of the central part of the Nile Cone. As can be noted in Figure 1a, the present-day slope is a part of large-scale clinoform and the shelf-slope break is moving toward the north direction with time. Besides the gravitational growth faults, the major structures in the area of interest are the southwest–northeast-trending Rosetta fault and the east-northeast–west-southwest-trending Nile Delta offshore anticline. Despite both were active during the Pliocene and Pleistocene, the depositional geometries of the upper Pliocene channels have not been affected (Samuel et al., 2003).

Our case study “Scarab field” is one of many Pliocene submarine channel systems in the WDDM concession (Figure 1b). The WDDM concession lies 50–100 km offshore in the northwest margin of the Nile cone in water depths of 250–850 m (Samuel et al., 2003). The Scarab field had been discovered in 1998 by the Scarab 1 and 2 exploration wells. Subsequently, the field is produced

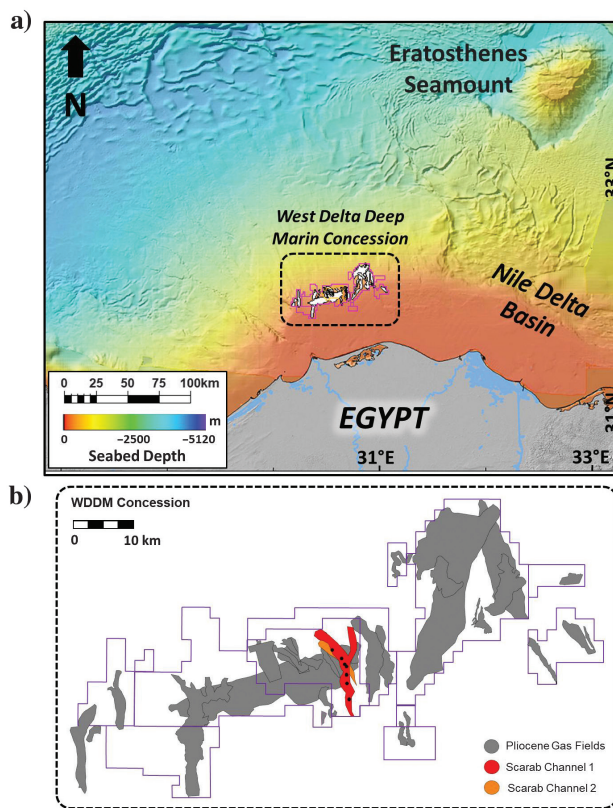


Figure 1. (a) Bathymetric map of the eastern Mediterranean region showing the location of the WDDM concession and (b) an index map showing the location of the Scarab channel system complex. Modified from Mohamed et al. (2014).

through the Scarab-Da, -Db, -Dc, -Dd, and -De development wells (Figure 2). The peak production reached 800 million standard cubic feet of gas per day to the domestic Egyptian market as Mohamed et al. (2014) mention. However, currently, the daily production rate is declining. The Scarab Canyon consists of two intersecting channels, namely, the Upper (Channel 1) and the Lower (Channel 2) Scarab channels. They are trending in different directions, but they still share similar depositional environments (Figure 2). Scarab's depositional system shows the complexity and a high degree of heterogeneity, reflecting the nature of its depositional processes. The details of the sedimentological story of the Scarab system have been discussed by El-Mowafy et al. (2018). According to the petrophysical analysis, the reservoir is characterized by a gross thickness of 170 m and that have 50 m of pay with an average porosity of 28% and average water saturation of 28%. The Upper channel (channel 1) is the main producer of the field, and so this study will be focused on it. Figure 3 shows an example of the well data in one of Scarab's wells.

Methods

To overcome the band-limited nature of the seismic data when predicting a reservoir property, the water saturation in our case, we designed a three-step workflow. This workflow started with seismic data conditioning and quality control. The second step was implementing stochastic inversion in a stratigraphic grid with a cell thickness of

1 ms. For the last step, we used the inversion output elastic volumes to train and validate a neural network to predict the water saturation in a 3D space. Figure 4 highlights the workflow's main steps.

Prior to the inversion, the conditioning for the seismic angle-stack data includes the time misalignment correction and amplitude balancing, and the details of these steps are listed by Mohamed et al. (2015). The well-to-seismic ties were performed with two wavelet sets: statistical and deterministic wavelets. The synthetic seismograms that used deterministic wavelet set were tied to seismic better than those that used statistical ones. Thus, it had been used for the inversion process.

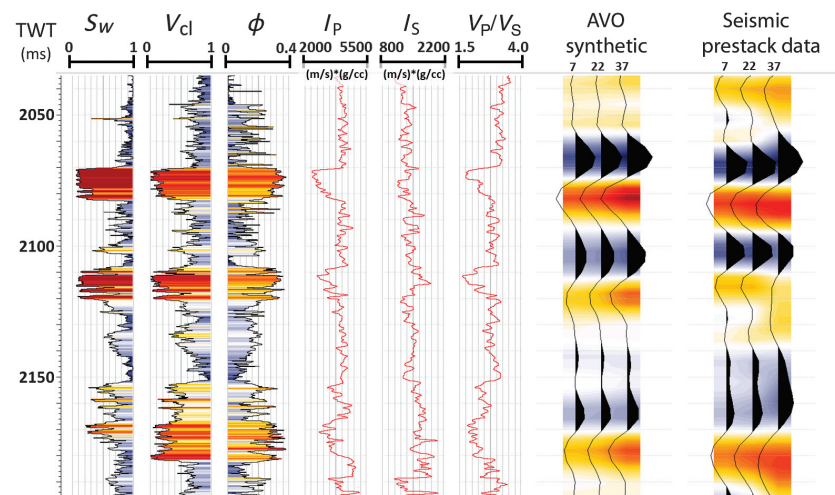


Figure 3. An example of the well-log data and the AVO synthetic compared with the actual seismic angle stacks at the Scarab 1 well location. The logs (from left to right) are water saturation (S_w), clay volume (V_{cl}), effective porosity (ϕ_{eff}), P-impedance, S-impedance, and V_p/V_s . The hot colors indicate sandstone, whereas gray represents shale. The polarity convention in this display denotes a decrease in the acoustic impedance by a peak.

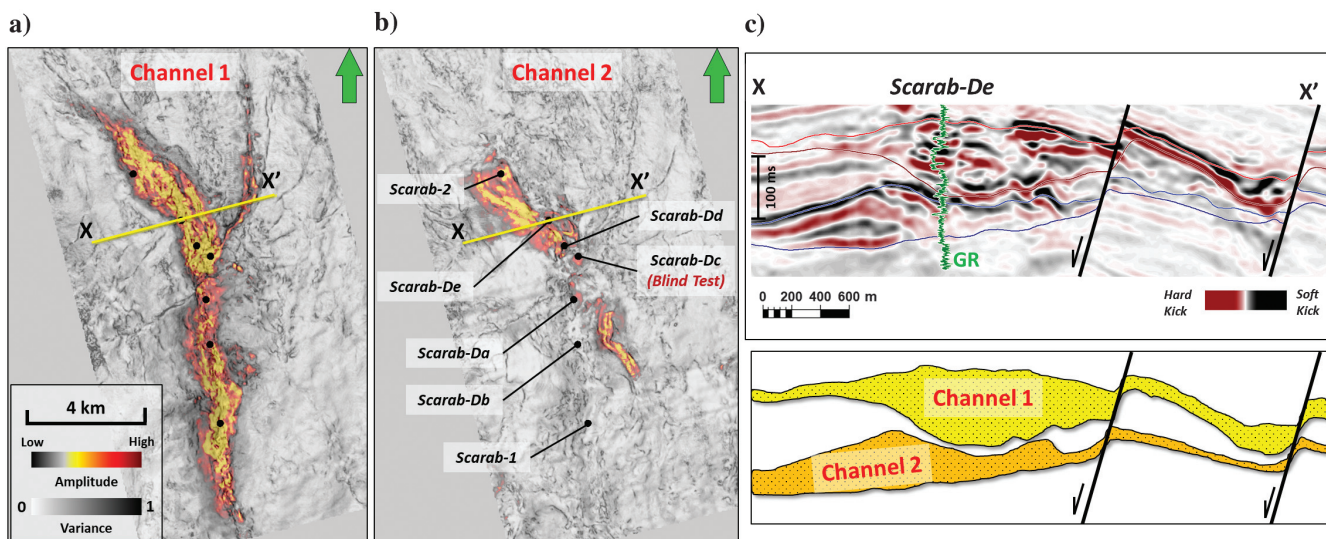


Figure 2. (a) Sum of positive amplitude maps over the channel 1 and (b) channel 2 overlain variance slices. (c) A seismic section through Scarab-de well location with the gamma-ray log and the corresponding schematic section illustrating the Scarab field sedimentology. The upper channel is younger and incised into the lower channel.

Geostatistical inversion

The geostatistical stochastic inversion algorithm is a combination of the Bayesian linearized amplitude versus angle inversion approached by [Buland and Omre \(2003\)](#) and the sequential Gaussian simulation (SGS) technique that, for example, is used by [Haas and Dubrule \(1994\)](#). Considering the assumptions described in [Escobar et al. \(2006\)](#), it calculates a joint posterior distribution for the P- and S-impedances, constrained by the seismic amplitudes. Then, it uses the SGS to decompose the joint posterior into a series of local Gaussian posterior distributions for each seismic trace that can be sampled sequentially to generate realizations of elastic properties ([Moyen and Doyen, 2009](#)). The mathematical explanation for the inversion algorithm and its assumptions is shown in Appendix A.

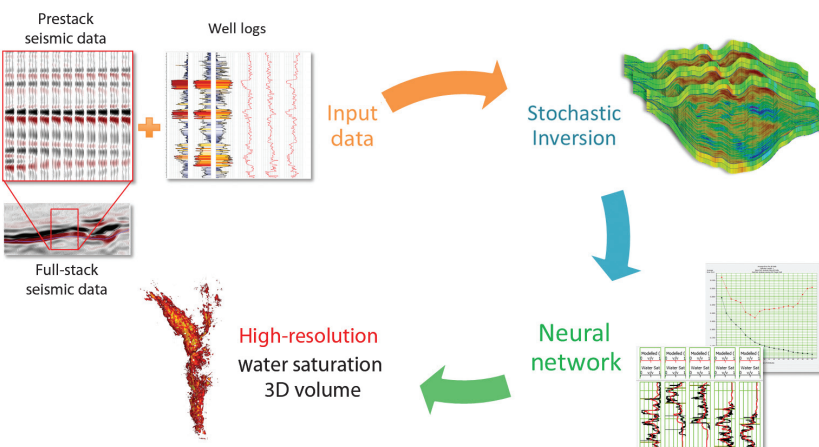


Figure 4. Flowchart generally outlining the steps of the high-resolution water-saturation prediction workflow.

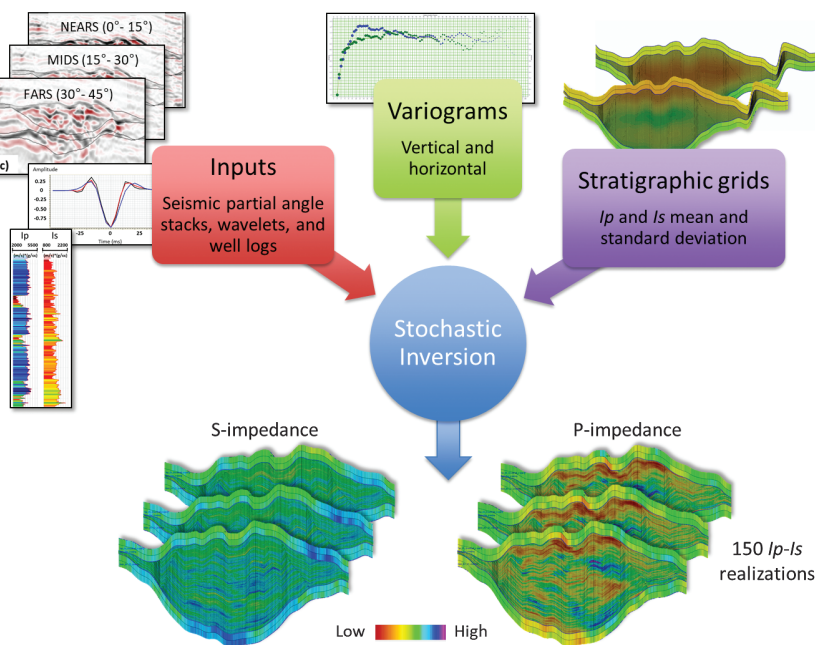


Figure 5. Flowchart showing a summary of the geostatistical inversion steps.

Practically, it addresses the “nonuniqueness problem” by producing a large range of inversion results, or high-frequency stochastic realizations, for a given input ([Bellatreche et al., 2017](#)). All of the realizations are valid solutions to the inverse problem, and each of them will honor the continuity that is expected using the input variograms. Among this range of results, the most likely result and therefore the uncertainty range can be estimated. The high-frequency component that comes from the variograms allows the inversion to be performed on a fine-scale grid (1 ms) instead of the normal seismic scale (4 ms). Consequently, the geostatistical inversion delivers high-frequency realizations of elastic properties including the P- and S-impedances, V_p/V_s , lambda-rho ($\lambda\rho$), and mu-rho ($\mu\rho$) volumes. In addition to the facies distribution and associated uncertainty volumes.

Figure 5 shows a summary of the steps of the geostatistical inversion method. The inversion main steps were as follows:

- Built a stratigraphic grid: We constructed a fine-scale grid inside the reservoir using the top and base of the Upper Channel horizons, and we populated the low-frequency P- and S-impedances using the inverse distance weighting algorithm. We have designed the micro-layers to follow the depositional model (i.e., proportional); therefore, the mean thickness was 1 ms within the reservoir and 4 ms above and below the reservoir.
- Assigned three angle-dependent deterministic wavelets for the three input seismic partial stacks. The three wavelets represented the near, mid, and far angles.
- Defined the prior vertical and horizontal variogram models within the stratigraphic grid. We computed the vertical variogram using the well logs and set the horizontal variogram to follow the geologic trend of the Scarab field.
- Computed the Bayesian joint posterior distribution of the elastic properties for every trace by combining the initial model, seismic prestack data, and well logs to be honored within the inversion.
- Created multiple P- and S-impedance realizations (150 realizations) for each trace by the sequential sampling of the joint posterior distribution.

Figure 6 shows the geostatistical inversion analysis at two well locations:

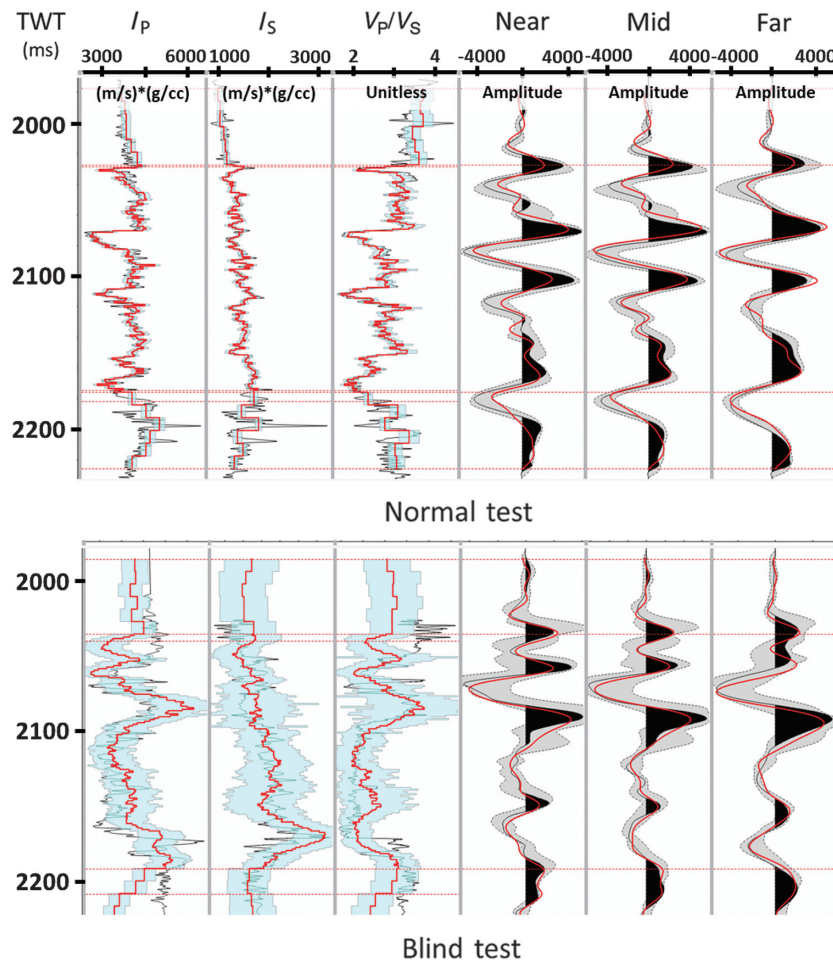


Figure 6. Geostatistical inversion analysis at two well locations. The upper is the Scarab 1 well, whereas the lower is the Scarab-Dc well (blind test). Note that the inversion results (red log) are restricted to the well data for Scarab 1; conversely, we have a wider range of possibilities for the blind well.

the Scarab 1 well and the Scarab-Dc well (blind test). At the blind-well location, we had a range of possibilities; on the other hand, at the other well locations, the inversion results were restricted to the well's values. Post the inversion, we computed the mean of the impedance realizations and the standard deviation as well. Also, we generated the facies probability (gas sand probability) volume using a multivariate probability distribution function (PDF), as shown in Figure 7.

Neural networks

In this study, we have tested two types of well-known neural networks: the most common neural network, the multilayer feed-forward neural network (MLFN), and PNN. As Hampson et al. (2001) mention that “the MLFN is the traditional network.” This type of network contains one or more of “hidden layers” between the input and output layers. Each layer consists of nodes (neurons), and the connection between the nodes of adjacent layers is set by weights. The algorithm (Appendix B) computes the weights for each layer that minimize the error between the output value and the training value (Table 1). In this study, we used the basic architecture that consists of three layers: the input, hidden, and output layers. For the input layer, the number of nodes is the same as the number of attributes.

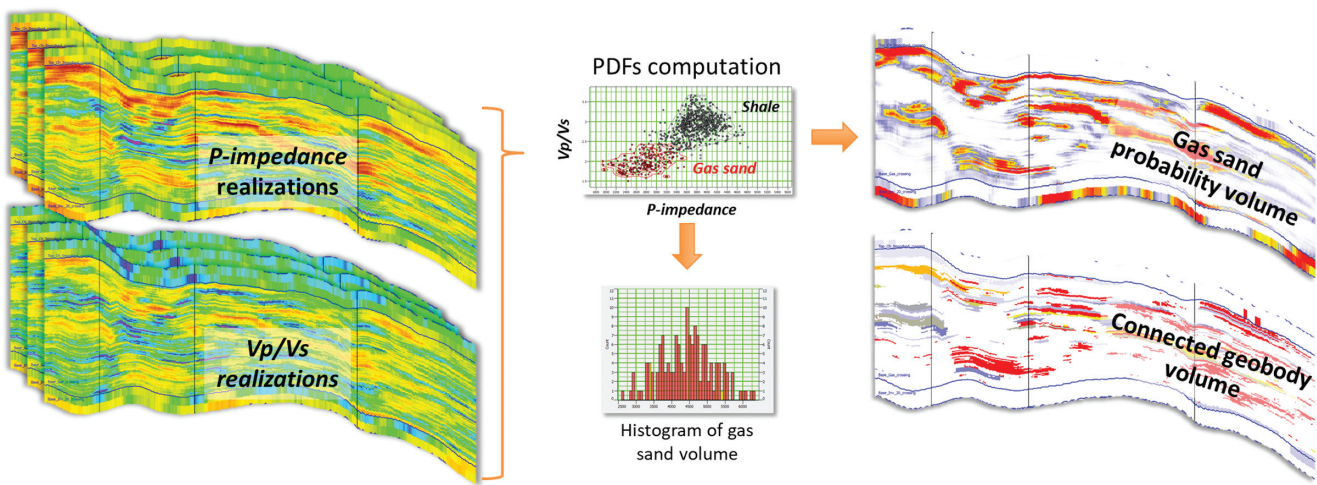


Figure 7. Vertical section intersecting three wells shows the P-impedance's three plausible scenarios: pessimistic (P10), most likely (P50), and optimistic (P90), based on the volume of pay. Using the rock-physics model that is generated from the AI and V_p/V_s logs, the histogram of the gas-sand volume is constructed from 150 facies realizations. On the far right, the same sections show the high gas-sand probability distribution (upper) and the connected sand volume (lower).

Conversely, the output layer consists of a single node because we were predicting a single property. The approach of this network is different than the PNN, which is considered as a “mathematical interpolation scheme,” but uses an NN architecture for its implementation (Hampson et al., 2001). For the network training, the PNN uses Gaussian weighting functions to fit the seismic attributes to the training samples. The Gaussian normal distribution is centered at each training sample (the mean), and the algorithm optimizes the standard deviation or the smoothness parameter, sigma, for each attribute. The mathematical explanations for those networks are shown in Appendix B.

Figure 8 illustrates the neural networks workflow; we have used the same workflow for both methods.

First of all, we started with the input data loading and quality control. The input data includes the well-log data (S_w log for each well), seismic full-stack, rms velocity, and geostatistical inverted volumes. We resampled the well logs at 1 ms to make sure that the well-log data were consistent with the stochastic inversion data. In the second step, we found the most effective set of attributes, which would predict the water saturation with the lowest prediction error. The attributes list includes internal attributes that are derived from the seismic full-stack data and external attributes, which are the rms velocity and the inversion volumes. The technique used here is called multilinear regression. Accordingly, the provided ordering and number of attributes will be used to train the neural network.

Table 1. List of order and number of attributes that are used to train and validate the PNN, and the MLFN. The training and validation errors are shown in the right two columns for each case.

Training and validation of the neural networks					
PNN			MLFN		
Attribute	Training error	Validation error	Attribute	Training error	Validation error
1 Sqrt (gas-sand probability)	0.199	0.212	Sqrt (gas-sand probability)	0.199	0.212
2 Sqrt (geobodies volume)	0.190	0.205	(MuRho P10) ²	0.190	0.201
3 1/(P-impedance P10)	0.186	0.199	1/(MuRho P50)	0.186	0.197
4 Frequency filter 5/10–15/20	0.183	0.198	1/(P-impedance P90)	0.183	0.196
5 1/(MuRho P50)	0.180	0.196	1 / (S-impedance P50)	0.181	0.194
6 (MuRho P10) ²	0.177	0.191	Log (gas-sand realization P90)	0.180	0.193
7 Frequency filter 35/40–45/50	0.174	0.189	Frequency filter 5/10–15/20	0.178	0.190
8 Log (gas-sand realization P50)	0.172	0.187	Frequency filter 35/40–45/50	0.176	0.188

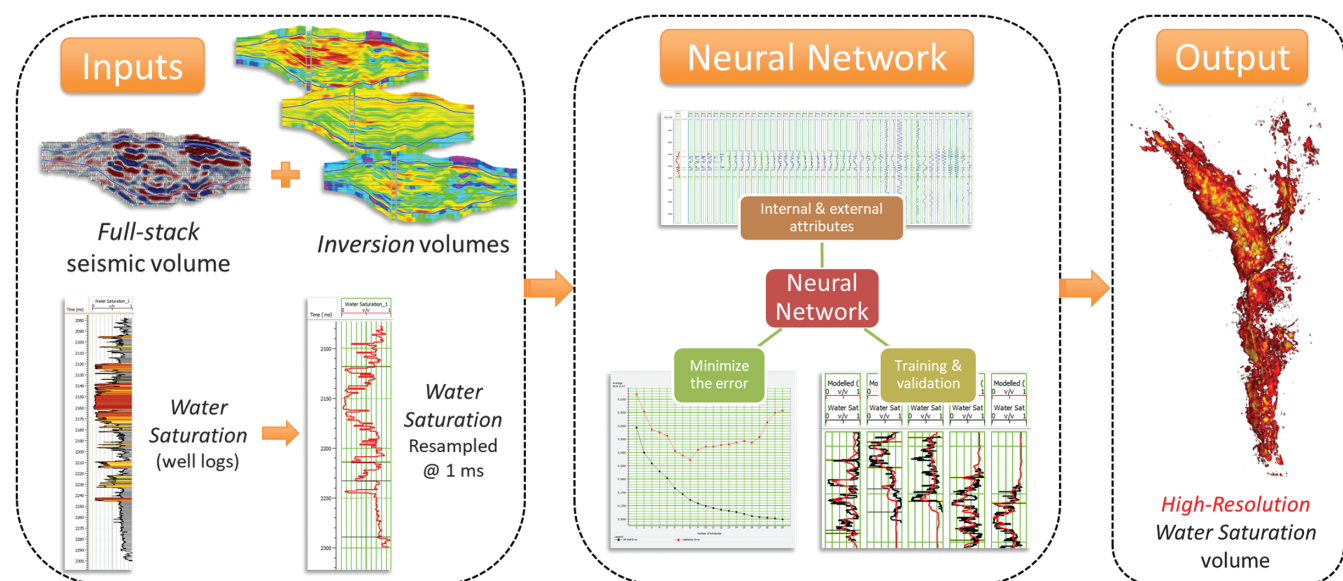


Figure 8. Flowchart showing a summary of neural network steps. The same workflow was applied to the MLFN and PNN methods.

Next, we tested the neural network algorithms. We first tested the PNN method following the workflow that had been provided by Hampson et al. (2001). After the training, there is the validation step, in which one-third of the well data were removed from the training step and then we predicted these well data blindly. This allowed us to find the number of statistically valid attributes. Table 1 shows the list of the order and types of the attributes that were used in training the network. In the last step, we applied the weights from the trained neural network to the 3D seismic and inversion volumes.

The second test was the MLFN algorithm. After the training and validation, once we had a good correlation at the well locations, we applied the MLFN to the whole 3D training volumes to predict the saturation. We then compared the output saturation volumes.

Results

The output from geostatistical inversion was a large number of stochastic realizations (150 realizations). From those volumes, we decided to export only the important realizations that represent; mean, P10, P50, and P90 cases for each of P-and S-wave impedances, V_P/V_S , $\lambda\rho$, $\mu\rho$, gas-sand probability, and the connected geobodies' volume. Accordingly, a total of 25 volumes were

exported, and all are sampled every 1 ms (1–1.5 m) inside the Upper Channel reservoir. These volumes are then used to train a neural network to predict the water saturation.

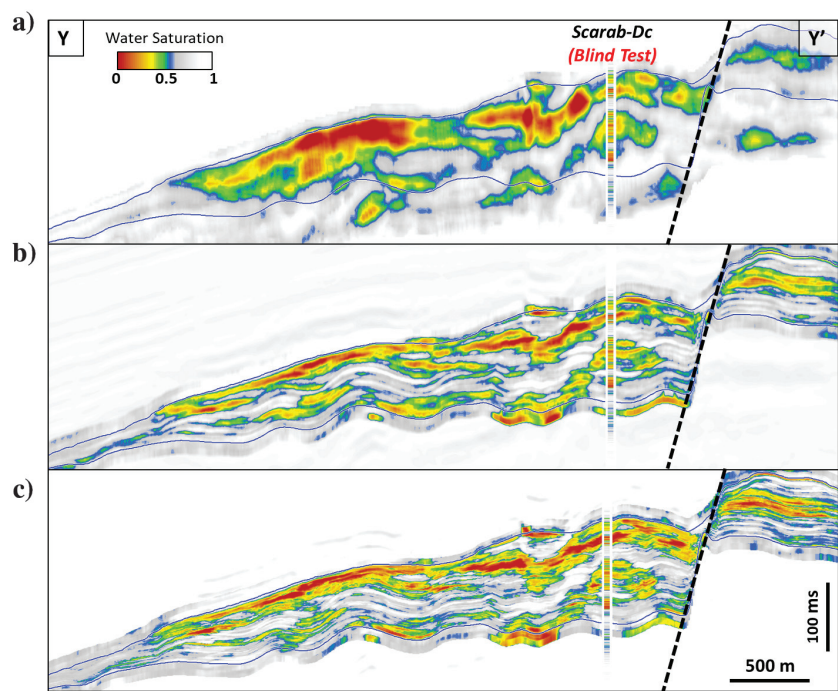


Figure 10. Comparison of water-saturation predictions for the same seismic line through the blind-well location: (a) PNN prediction from the deterministic inversion that is presented previously by Mohamed et al. (2014), (b) PNN prediction from the geostatistical inversion, and (c) MLFN prediction from the geostatistical inversion. Note the high resolution obtained when we applied MLFN. The direction of the line will be shown in Figure 11.

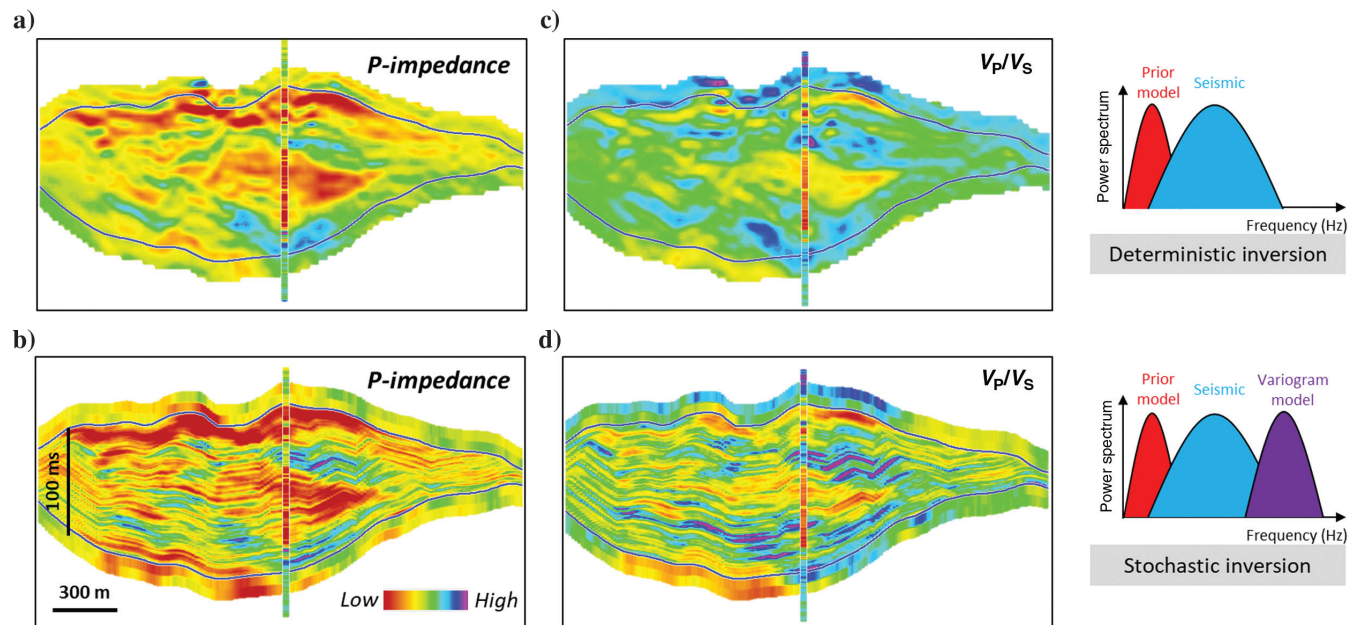


Figure 9. Comparison of deterministic (upper) and high-resolution geostatistical inversion (lower) results in the acoustic-impedance domain: (a and b) P-impedance sections and (c and d) V_P/V_S sections through the blind-well location. The deterministic results are sampled at 4 ms, whereas the stochastic-inversion results are sampled at 1 ms. Geostatistical inversion provides more detail than does deterministic inversion and therefore enabled detailed reservoir characterization.

The blind-well test is a good indication of the quality of the techniques used in the study. Figure 9 shows the results of the deterministic and geostatistical inversion for P-impedance and V_P/V_S at the blind-well (Scarab Dc) location. When compared with the deterministic inversion, different known sandy reservoir units are now resolved in the stochastic inversion products.

The output volumes from the PNN and MLFN methods were high-resolution Sw volumes that within the upper channel reservoir. For the water-saturation prediction, Figure 10 compares the different predictions

for the same seismic line through the blind-well location. Figure 10a is the PNN prediction from the deterministic inversion that presented previously by Mohamed et al. (2014). Figure 10b is the PNN prediction from the geostatistical inversion, and, finally, Figure 10c is the MLFN prediction from the geostatistical inversion. The last two volumes are sampled every 1 ms inside the reservoir. Figure 11 shows the saturation maps for the three volumes.

The PNN prediction from the deterministic inversion result shows a smoothed, or more averaged, water-saturation result. Conversely, the PNN from the geostatistical inversion result retains more of the high-frequency content as exhibited by the water-saturation logs at the blind-well location. The MLFN prediction from the geostatistical inversion is even better: It shows a very high resolution in both directions, vertically and laterally. The very fine details of the water saturation are resolved inside the reservoir and match the blind nicely. This degree of resolution is required in estimating flow continuity and barriers. In a quantitative way, the normalized correlations between the actual saturation log and predicted values from the three methods are 0.78, 0.86, and 0.87, respectively. In the map view, the last method shows more gases than the other methods, which are very consistent with the field-production data. This referred to the ability to see more of the thin-bedded reservoirs.

The benefits of this improved vertical and lateral resolution are evident on a newly drilled well post the study — let us call it well-X — which was designed to drain the eastern branch of the upper channel. Figure 12 shows the high-resolution water-saturation prediction, using MLFN, at the well-X location. Note the excellent agreement of the well results with the water-saturation prediction. Quantitatively, the correlation between the provisional saturation log and predicted saturation is 0.89. In Figure 12c, we have used the animation to provide an insight vision of the saturation 3D distribution and to demonstrate the match between the volume and the new well.

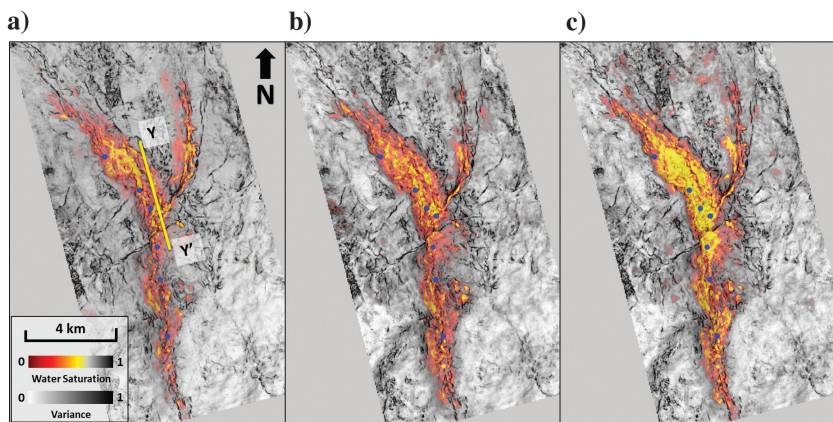


Figure 11. Comparison of water-saturation predictions in a map view for (a) PNN prediction from the deterministic inversion that presented previously by Mohamed et al. (2014), (b) PNN prediction from the geostatistical inversion, and (c) MLFN prediction from the geostatistical inversion. The larger gas volume (c) is more consistent with the production data.

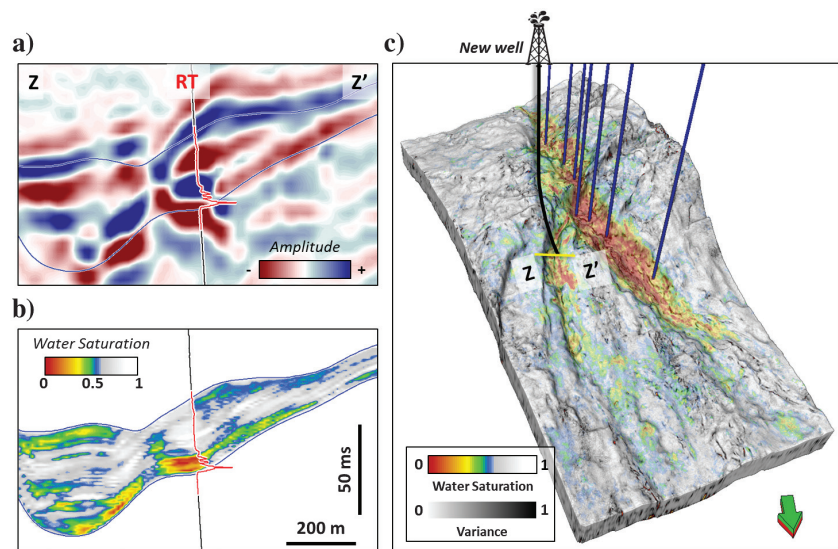


Figure 12. (a) Seismic section and (b) water-saturation section with the resistivity log through the new well that was drilled post the study to drain the eastern branch of the upper channel. (c) The 3D view of the gas sand geobodies from the high-resolution water-saturation volume (from MLFN). Note the excellent agreement of the well results with the water-saturation prediction, which indicates that the gas sand would exist only in the lower layer; conversely, the seismic alone, would be misleading (supplementary information can be accessed through the following link: [S1.mov](#)).

Conclusion

Seismic vertical resolution used to be a major obstacle that challenged the accurate prediction of pore-fluid properties, especially where the reservoir is heterogeneous and falls partially below the seismic tuning thickness. In this study, we

designed a new workflow that implements the geostatistical inversion and neural network methods to overcome the limitation of seismic data when predicting a reservoir property. The geostatistical inversion showed a superior result over the deterministic inversion, provided a high level of detail, and enhanced the lateral continuity. Then, two different neural network methods were tested using the results of the geostatistical inversion. The results from both methods were very encouraging. However, the results suggest that MLFN is better than PNN. That was shown quantitatively using blind-well analysis. The main downside with this approach is that the final values of the weights are dependent on the value of the initial random weights. This means that the results can be varied slightly from one run to another. Nevertheless, it is still faster than PNN. Moreover, away from the well control, the MLFN results show lateral water-saturation variability expected in this stratigraphically controlled reservoir. Despite the proposed workflow proved its validity and accuracy in predicting the saturation, it still needs at least three wells to be applied successfully. This makes it better suited to the development and near-field exploration phases.

Acknowledgments

We would like to thank *Interpretation*'s editor K. Marfurt and the anonymous reviewers for their constructive suggestions. We would also like to thank the Egyptian General Petroleum Corporation and the Rashid Petroleum Company (RASHPETCO) for providing the data and for permission to publish this study.

Data and materials availability

Data associated with this research are confidential and cannot be released.

Appendix A

Geostatistical inversion

[Escobar et al. \(2006\)](#) propose the geostatistical stochastic inversion algorithm, using a Bayesian framework and a linearized approximation of the Zoeppritz equation, to calculate a joint posterior distribution for the acoustic and shear impedances. For a single interface, the approximation of the angle-variant reflectivity is ([Fatti et al., 1994](#))

$$r_\theta \approx \frac{1}{2\cos^2\theta} \Delta \ln(I_P) - 4 \frac{\overline{I_S}^2}{\overline{I_P}^2} \sin^2\theta \Delta \ln(I_S), \quad (\text{A-1})$$

where I_P and I_S are the acoustic and shear impedances, respectively. And for the stratigraphic grid, the equation will be extended to a full vertical column (i) of layers, where the logarithms of the I_P and I_S are stored in a vector (\mathbf{m}_i). The reflectivity series will be

$$\mathbf{r}_{i,\theta} \approx \mathbf{A}_{i,\theta} \mathbf{m}_i, \quad (\text{A-2})$$

where $\mathbf{A}_{i,\theta}$ differences $\ln(I_P)$ and $\ln(I_S)$ and multiplies them with the AVA coefficients (i.e., coefficients of

equation [A-1](#)). If we assume that the squared impedance ratios are known, then the equation is linear in log impedances. A postprocessing step is required to overcome this assumption. Without this step, a mismatch between the input seismic data and the synthetics would occur. The correction step will be applied to each trace and each realization after the inversion. Using the initial impedance ratio, the simulated reflectivities are corrected to match the computed reflectivities.

Following the work of [Buland and Omre \(2003\)](#), the inverse problem can be expressed in a Bayesian framework with Gaussian PDFs. The likelihood of seismic data \mathbf{s} is

$$p(\mathbf{s}|\mathbf{m}) \propto \exp\left(-\frac{1}{2} \sum_{\theta} \sum_i (\mathbf{s}_{i,\theta} - \mathbf{G}_{i,\theta} \mathbf{m}_i)^T \mathbf{C}_{si,\theta}^{-1} (\mathbf{s}_{i,\theta} - \mathbf{G}_{i,\theta} \mathbf{m}_i)\right), \quad (\text{A-3})$$

where $\mathbf{C}_{si,\theta}$ are the noise covariance matrices and $\mathbf{G}_{i,\theta}$ are the rectangular matrices that group together $\mathbf{A}_{i,\theta}$ with the wavelet convolution and transform the irregular layers (model trace) into regular samples (seismic trace). The expression of the Gaussian prior PDF for \mathbf{m} is

$$p(\mathbf{m}) \propto \exp\left(-\frac{1}{2} (\mathbf{m} - \mu_m)^T \mathbf{C}_m^{-1} (\mathbf{m} - \mu_m)\right), \quad (\text{A-4})$$

where μ_m is the prior mean, \mathbf{C}_m is the prior covariance matrix, and \mathbf{C}_m depends on prior variograms and vertical correlations. When a logged well is intersecting a trace, an additional likelihood term will be added. By the combination of equations [A-3](#) and [A-4](#), the Gaussian posterior PDF $p(\mathbf{m}|\mathbf{s})$ will be constructed. Then, an SGS algorithm will be used to decompose trace by trace the posterior PDF into local PDFs. These PDFs are then sampled to generate the realizations of the elastic parameters ([Escobar et al., 2006](#)).

Appendix B

Multilayer feed-forward neural network

In this study, we used the basic architecture of the MLFN ([Figure B-1](#)) that consists of three layers: the input, hidden, and output layers. Each layer consists of nodes (neurons), and the connection between the nodes of adjacent layers is set by weights. The training process

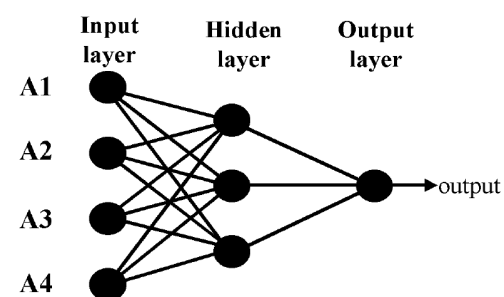


Figure B-1. The basic neural network architecture ([Todorov, 2000](#)).

aims to find the optimum weights for those nodes (Hampson et al., 2001). Mathematically, the input signals are multiplied by the synaptic (connection) weights; these weighted signals are then summed and have a non-linear (activation) function applied to them as follows (Todorov, 2000):

$$y = f \left(\sum_{i=0}^{n-1} x_i w_i + w_n \right), \quad (\text{B-1})$$

where y is the neuron's output; x_i is the neuron inputs; w_i is the synaptic (connection) weights; $i = 1, \dots, n - 1$; w_n is a constant (bias); and f is an activation function. The weights are optimized by minimizing the prediction error. To avoid trapping in the local minima, MLFN uses a combination of simulated annealing and conjugate-gradient analysis to find the global minimum.

Probabilistic neural network

PNN uses a different approach than MLFN: It uses Gaussian weighting functions to fit the seismic attributes (x) to the training samples (x_i). Each training sample represents the mean of a normal (Gaussian) distribution, and the algorithm finds the best standard deviation or the smoothing parameter σ_j . The fundamental equation of the general regression PNN is (Todorov, 2000)

$$y'(x) = \frac{\sum_{i=1}^n y_i \exp(-D(x, x_i))}{\sum_{i=1}^n \exp(-D(x, x_i))}, \quad (\text{B-2})$$

where n is the total number of training samples, y_i represents the measured target log values, y' is the new log value, and $D(x, x_i)$ is given by

$$D(x, x_i) = \sum_{j=1}^p \left(\frac{x_j - x_{ij}}{\sigma_j} \right)^2. \quad (\text{B-3})$$

The term $D(x, x_i)$ represents the distance between the input seismic attribute (x) and each of the training points (x_i), and the number of seismic attributes is (p). The smoothing parameter (σ_j) varies for each attribute. To find the best set of smoothing parameters, crossvalidation is implemented, in which part of the data is left out of the training data (Hampson et al., 2001). Then, the validation error is minimized using the conjugate gradient method (Todorov, 2000).

References

- Aal, A. A., A. El-Barkooky, M. Gerrits, H. Meyer, M. Schwander, and H. Zaki, 2001, Tectonic evolution of the Eastern Mediterranean basin and its significance for the hydrocarbon prospectivity of the Nile Delta deepwater area: *GeoArabia*, **V6**, 363–384.
- Araman, A., T. Cadoret, L. Pernia, D. Minken, and R. Moyen, 2011, Geostatistical inversion for 3D confidence evaluation of facies prediction: A Gulf of Guinea example: 81st Annual International Meeting, SEG, Expanded Abstracts, 1729–1733, doi: [10.1190/1.3627539](https://doi.org/10.1190/1.3627539).
- Bellatreche, K., A. Couch, and R. Evans, 2017, Detailed seismic lithofluid distribution using Bayesian stochastic inversion for a thinly bedded reservoir: A case study over Huntington UK Central North Sea: *Interpretation*, **5**, no. 3, SL25–SL32, doi: [10.1190/INT-2016-0161.1](https://doi.org/10.1190/INT-2016-0161.1).
- Buland, A., and H. Omre, 2003, Bayesian linearized AVO inversion: *Geophysics*, **68**, 185–198, doi: [10.1190/1.1543206](https://doi.org/10.1190/1.1543206).
- Cozzi, A., A. Cascone, L. Bertelli, F. Bertello, S. Brandoles, M. Minervini, P. Ronchi, R. Ruspi, and H. Harby, 2018, Zohr giant gas discovery: A paradigm shift in Nile Delta and East Mediterranean exploration: Discovery Thinking Forum AAPG/SEG International Conference and Exhibition.
- Dumitrescu, C. C., and L. Lines, 2009, Characterization of heavy oil reservoir using V_p/V_s ratio and neural network analysis: CSPG-CSEG-CWLS Convention Abstracts, 646–648.
- El-Mowafy, H. Z., M. Ibrahim, and D. Dunlap, 2018, Unlocking gas reserves in bypassed stratigraphic traps in a deepwater brownfield using prestack seismic inversion: A case study from offshore Nile Delta, Egypt: The Leading Edge, **37**, 502–509, doi: [10.1190/tle37070502.1](https://doi.org/10.1190/tle37070502.1).
- Escobar, I., P. Williamson, A. Cherrett, P. Doyen, R. Borrard, R. Moyen, and T. Crozat, 2006, Fast geostatistical stochastic inversion in a stratigraphic grid: 76th Annual International Meeting, SEG, Expanded Abstracts, 2067–2071, doi: [10.1190/1.2369943](https://doi.org/10.1190/1.2369943).
- Fatti, J. L., G. Smith, P. Vail, P. Strauss, and P. Levitt, 1994, Detection of gas in sandstone reservoirs using AVO analysis: A 3-D seismic case history using the geostack technique: *Geophysics*, **59**, 1362–1376, doi: [10.1190/1.1443695](https://doi.org/10.1190/1.1443695).
- Haas, A., and O. Dubrule, 1994, Geostatistical inversion: A sequential method of stochastic reservoir modeling constrained by seismic data: *First Break*, **12**, 561–569, doi: [10.3997/1365-2397.1994034](https://doi.org/10.3997/1365-2397.1994034).
- Hampson, D. P., J. Schuelke, and J. Quirein, 2001, Use of multi-attribute transforms to predict log properties from seismic data: *Geophysics*, **66**, 220–236, doi: [10.1190/1.1444899](https://doi.org/10.1190/1.1444899).
- Herrera, V. M., B. Russell, and A. Flores, 2006, Neural networks in reservoir characterization: The Leading Edge, **25**, 402–411, doi: [10.1190/1.2193208](https://doi.org/10.1190/1.2193208).
- Kirschbaum, M. A., C. Schenk, R. Charpentier, T. Klett, M. Brownfield, J. Pitman, T. Cook, and M. Tennyson, 2010, Assessment of undiscovered oil and gas resources of the Nile Delta Basin Province, eastern Mediterranean: U.S. Geological Survey Fact Sheet, 2010–3027.
- Mohamed, I. A., H. El-Mowafy, and M. Fathy, 2015, Prediction of elastic properties using seismic prestack inversion and neural network analysis: *Interpretation*, **3**, no. 2, T57–T68, doi: [10.1190/INT-2014-0139.1](https://doi.org/10.1190/INT-2014-0139.1).
- Mohamed, I. A., H. El-Mowafy, D. Kamel, and M. Heikal, 2014, Prestack seismic inversion versus neural-network analysis: A case study in the Scarab field offshore Nile Delta, Egypt: The Leading Edge, **33**, 498–506, doi: [10.1190/tle33050498.1](https://doi.org/10.1190/tle33050498.1).

- Mohamed, I. A., O. Shenkar, and H. Mahmoud, 2017, Understanding reservoir heterogeneity through water-saturation prediction via neural network: A case study from offshore Nile Delta: *The Leading Edge*, **36**, 298–303, doi: [10.1190/tle36040298.1](https://doi.org/10.1190/tle36040298.1).
- Moyen, R., and P. Doyen, 2009, Reservoir connectivity uncertainty from stochastic seismic inversion: 79th Annual International Meeting, SEG, Expanded Abstracts, 2378–2382, doi: [10.1190/1.3255337](https://doi.org/10.1190/1.3255337).
- Pereira, F. C., T. Holden, M. Ibrahim, and E. Porto, 2017, Geostatistical reservoir characterization in Barracuda field, Campos Basin: A case study: 15th International Congress of the Brazilian Geophysical Society, 1165–1169.
- Samantaray, S., R. Moyen, J. Michel, A. Bouziat, A. Yahia, and N. Al Zaabi, 2014, Seismic-based stochastic porosity prediction in a Giant field: A fine-scale quantitative approach in carbonates: EAGE, International Petroleum Technology Conference.
- Samuel, A., B. Kneller, S. Raslan, S. Andy, and C. Parsons, 2003, Prolific deep-marine slope channels of the Nile Delta, Egypt: AAPG Bulletin, **87**, 541–560, doi: [10.1306/1105021094](https://doi.org/10.1306/1105021094).
- Todorov, T. I., 2000, Integration of 3C-3D seismic data and well logs for rock property estimation: M.S. thesis, University of Calgary.



Islam A. Mohamed received a B.S. (2007) with honors and an M.S. (2014) in geophysics from the Al-Azhar University, Cairo. Currently, he is pursuing his Ph.D. in geophysics. He joined Rashpetco (Shell-JV) in 2008 as a geophysicist with a specific focus on quantitative interpretation methods. His research interests include quantitative seismic interpretation and machine-learning applications for reservoir characterization. He is an active member of SEG and AAPG.



Mahmoud Hemdan received a B.S. (2006) in geology and geophysics from Ain Shams University, Egypt. He joined the Rashpetco subsurface team in 2007 as a staff geophysicist. He was a part of integrated team responsible for the development of large gas fields in the offshore Mediterranean and also for generating new prospects.

His research interests include the combined use of seismic interpretation, rock physics, reservoir characterization, and uncertainty assessment in frontier exploration areas.



Ahmed Hosny received a B.S. (2009) in geophysics and an M.S. (2014) from Ain Shams University. His M.S. research project was on rock physics and seismic inversion. After six years of industrial experience, he successfully completed his research project on seismic time lapse (4D), and he received a Ph.D. (2017) from Ain Shams University. During his 10-year career experience, he has worked on seismic acquisition, processing, interpretation, and inversion. He joined Petrographic in 2010; currently, he works for Rashpetco.



Mohamed Rashidy received a B.S. (2009) in geophysics from the Suez Canal University, Egypt. He joined Rashpetco in 2011 as a well-site geologist then as a well-log analyst. In 2014, he joined the development team as a development geophysicist. He is the area geophysicist of three large gas fields in the offshore Mediterranean. His research interests include interpretation and reservoir characterization.